Astronomy & Astrophysics

GRB 070311: a direct link between the prompt emission and the afterglow[*]

C. Guidorzi[1,2], S. D. Vergani[3,4], S. Sazonov[5,6], S. Covino[2], D. Malesani[7], S. Molkov[6], E. Palazzi[8], P. Romano[1,2], S. Campana[2], G. Chincarini[1,2], D. Fugazza[1,2], A. Moretti[2], G. Tagliaferri[2], A. Llorente[9], J. Gorosabel[10], L. A. Antonelli[11,12], M. Capalbi[12], G. Cusumano[13], P. D'Avanzo[2,14], V. Mangano[13], N. Masetti[8], E. Meurs[3,4], T. Mineo[13], E. Molinari[2], D. C. Morris[15], L. Nicastro[8], K. L. Page[16], M. Perri[12], B. Sbarufatti[13], G. Stratta[12], R. Sunyaev[5,6], E. Troja[13,16], and F. M. Zerbi[2]

[1] Università degli studi di Milano-Bicocca, Dipartimento di Fisica, piazza delle Scienze 3, 20126 Milano, Italy
    e-mail: cristiano.guidorzi@brera.inaf.it
[2] INAF - Osservatorio Astronomico di Brera, via E. Bianchi 46, 23807 Merate (LC), Italy
[3] Dunsink Observatory – DIAS, 31 Fitzwilliam Street, Dublin 2, Ireland
[4] School of Physical Sciences and NCPST, Dublin City University, Dublin 9, Ireland
[5] Max-Planck-Institut für Astrophysik, Karl-Schwarzschild-Str. 1, 85740 Garching bei München, Germany
[6] Space Research Institute, Russian Academy of Sciences, Profsoyuznaya 84/32, 117997 Moscow, Russia
[7] Dark Cosmology Centre, Niels Bohr Institute, University of Copenhagen, Juliane Maries vej 30, 2100 København Ø, Denmark
[8] INAF - Istituto di Astrofisica Spaziale e Fisica Cosmica, Sezione di Bologna, via P. Gobetti 101, 40129 Bologna, Italy
[9] XMM-Newton Science Operations Centre, European Space Agency, Villafranca del Castillo, PO Box 50727, 28080 Madrid, Spain
[10] Instituto de Astrofísica de Andalucía (IAA-CSIC), Apartado de Correos, 3.004, 18080 Granada, Spain
[11] INAF - Osservatorio Astronomico di Roma, via Frascati 33, 00040, Monte Porzio Catone, Italy
[12] ASI Science Data Center, via G. Galilei, 00044 Frascati (Roma), Italy[**]
[13] INAF - Istituto di Astrofisica Spaziale e Fisica Cosmica, Sezione di Palermo, via U. La Malfa 153, 90146 Palermo, Italy
[14] Università dell'Insubria, Dipartimento di Fisica e Matematica, via Valleggio 11, 22100 Como, Italy
[15] Department of Astronomy and Astrophysics, Pennsylvania State University, University Park, PA, USA
[16] Department of Physics and Astronomy, University of Leicester, Leicester LE1 7RH, UK

ABSTRACT

Context. The prompt emission of gamma-ray bursts is mostly thought to be produced in internal shocks of relativistic shells emitted by the progenitor at different times, whereas the late multi-band afterglow is interpreted as the synchrotron emission of electrons swept up by the fireball expanding through the surrounding interstellar medium. The short timescale variability observed in flares superimposed on the X-ray/optical afterglow of several bursts, recently made possible by Swift, has been interpreted as evidence for prolonged activity of the inner engine through internal shocks. Yet, it is not clear whether this applies to all the observed bursts and, in particular, whether the bursts exhibiting single γ-ray pulses with no short timescale variability at late times could also be entirely interpreted as external shocks.
Aims. We present prompt γ-ray, early NIR/optical, late optical and X-ray observations of the peculiar GRB 070311 discovered by INTEGRAL, in order to gain clues on the mechanisms responsible for the prompt γ-ray pulse as well as for the early and late multi-band afterglow of GRB 070311.
Methods. We fitted with empirical functions the gamma-ray and optical light curves and scaled the result to the late time X-rays.
Results. The H-band light curve taken by REM shows two pulses peaking 80 and 140 s after the peak of the γ-ray burst and possibly accompanied by a faint γ-ray tail. Remarkably, the late optical and X-ray afterglow underwent a major rebrightening between 3×10^4 and 2×10^5 s after the burst with an X-ray fluence comparable with that of the prompt emission extrapolated in the same band. Notably, the time profile of the late rebrightening can be described as the combination of a time-rescaled version of the prompt γ-ray pulse and an underlying power law.
Conclusions. This result supports a common origin for both prompt and late X-ray/optical afterglow rebrightening of GRB 070311 within the external shock scenario. The main fireball would be responsible for the prompt emission, while a second shell would produce the rebrightening when impacting the leading blastwave in a refreshed shock.

Key words. gamma rays: bursts – X-rays: individuals: GRB 070311

1. Introduction

The bewildering variety of the long γ-ray prompt emission profiles of gamma-ray bursts (GRBs) has been puzzling

astronomers since their discovery (e.g. see Fishman & Meegan 1995, for a review). Among the most important open issues, at present, two are still debated. Firstly, how long does the central engine remain active? Does the emission consist of a single episode or a temporal sequence of events with interspersed quiescent periods? Secondly, after the discovery of the delayed multi-band long-lasting emission called "afterglow", made

---

possible for the first time by BeppoSAX ten years ago (Costa et al. 1997), a general consensus on the emission mechanisms of both the prompt and the afterglow emission is still missing, even though for the latter synchrotron radiation by a population of shocked electrons proved to be successful in accounting for a number of spectral and temporal evolution properties (e.g., Mészáros 2006). Gaining clues on these issues may help to shed light on the nature of the progenitors and the circumburst environment.

The advent of Swift (Gehrels et al. 2004) has allowed the study of multi-band afterglows as early as $\sim 10^2$ s after the prompt event, exploring a previously unknown time domain. Both optical and X-ray light curves have shown unexpected behaviours that still lack a solid agreed theoretical explanation. Among the impressive discoveries by Swift concerning the long GRBs, here we mention the canonical behaviour of steep-shallow-normal decay characterising most of the early X-ray afterglows, as well as the occurrence of X-ray flares in $\sim 50\%$ of them (see Zhang 2007, for a review up to date).

A number of different interpretations of the shallow decay phase experienced by the X-ray afterglows of a sizeable fraction of Swift bursts (Tagliaferri et al. 2005; O'Brien et al. 2006; Nousek et al. 2006; Zhang et al. 2006) have been proposed. They can be broadly classified according to the mechanism that is invoked: internal (IS; e.g. Rees & Mészáros 1994; Kobayashi et al. 1997) or external shocks (ES; e.g. Rees & Mészáros 1992; Shaviv & Dar 1995; Fenimore et al. 1996; Dermer & Mitman 1999). For instance, within the IS model, the shallow decay phase could be the result of low velocity contrast distribution wind of slow shells emitted soon after the fast ones (Granot & Kumar 2006). According to alternative ES interpretations, it could be the result of delayed energy injection into the fireball, either in the form of freshly ejected material from late engine activity ("refreshed shock scenario"; Rees & Mészáros 1998), or by the collision of a wind of low velocity contrast shells catching up with the fireball (Zhang & Mészáros 2001). More generally, the shallow decay could be the result of a "late prompt" emission, i.e. the same mechanism responsible for the γ-ray pulses of the prompt would be at work through later shells with decreasing bulk Lorentz factors (Ghisellini et al. 2007). Overall, a consensus is still missing, mainly due to the large variety of behaviours observed: in some cases, there is no spectral evolution across the break in the light curve marking the end of the shallow phase, compatible with the expectations from an external origin of the shocks, while for other GRBs the opposite is true (Liang et al. 2007).

Likewise, X-ray flares have been interpreted as the result of late internal dissipation rather than due to ES, one of the main arguments being their short timescales at late times, $\Delta t/t \ll 1$ (Burrows et al. 2005; Falcone et al. 2006; Romano et al. 2006; Chincarini et al. 2007; Lazzati & Perna 2007), whereas an ES origin would require increasing timescales (Fenimore et al. 1996; although see also Dermer 2007b).

Another debated topic concerns the presence of optical brightening contemporaneous with the prompt emission or occurring in the first $1-2$ h. A variety of mechanisms have been proposed to explain this, such as reverberation of the prompt emission radiation (GRB 050820A: Vestrand et al. 2006), reverse shock (GRB 990123: Akerlof et al. 1999), refreshed shocks and/or energy injection (e.g. GRB 021004: Fox et al. 2003; GRB 050820A: Cenko et al. 2006; GRB 060206: Wozniak et al. 2006; Monfardini et al. 2006), onset of the ES (GRB 060206 and GRB 060210: Stanek et al. 2007; GRB 060418 and GRB 060607A: Molinari et al. 2007), and

large angle emission (GRB 990123: Panaitescu & Kumar 2007). It is likely that the interplay of the many processes active after the GRB explosion may all affect the optical light curves, creating the rich variety of observed behaviours.

While GRBs with complex multi-peaked time profiles displaying no pulse width evolution with time seem to be explained more naturally through the mutual interaction of a wind of shells emitted at different times with different Lorentz factors (IS model), a single fast rise exponential decay (FRED; Fishman & Meegan 1995) profile can still match the expectations of a single shell sweeping up the interstellar medium (ISM) (Fenimore et al. 1996). In this scenario, the kinetic energy of a single ultra-relativistic shell is converted into internal energy of the swept-up ISM; the shocked electrons radiate via synchrotron emission and inverse Compton scattering. In the simplest case of a thin shell ploughing into the ISM and emitting for a short time, the expected time profile of the γ-ray prompt emission is that of a single pulse with fast rise and slow decay. The cooling timescale of electrons is negligible with respect to the hydrodynamical timescale in most cases (Sari & Piran 1997). As a consequence, the rise time is determined by the emission time given by the crossing time of the shell by the reverse shock, while the decay time is dominated by the angular spreading timescale.

In this paper we report on the γ-ray, X-ray and optical observations of GRB 070311, whose time profile is typical of a FRED. In particular, we focus on some properties shared by the γ-ray and optical prompt emission and the late optical and X-ray afterglow in the light of the refreshed shock scenario.

The paper is organised as follows: in Sects. 2 and 3 we describe the observations and the data reduction and analysis, respectively. Multiwavelength timing and spectral analysis of both the prompt and the afterglow emission is presented in Sect. 4. In Sect. 5 we discuss our results. Finally, in Sect. 6 we summarise our findings and conclusions.

Throughout the paper, times are given relative to the onset time of the GRB, which corresponds to 45 s prior to the INTEGRAL/IBAS trigger time, and the convention $F(\nu, t) \propto \nu^{-\beta} t^{-\alpha}$ has been followed, where the energy index β is related to the photon index $\Gamma = \beta + 1$.

All the quoted errors are given at a 90% confidence level for one interesting parameter ($\Delta\chi^2 = 2.706$), unless otherwise stated.

2. Observations

GRB 070311 triggered the INTEGRAL/IBAS in IBIS/ISGRI data on 2007 March 11 at 01:52:50 UT and it was localised at RA = $05^h50^m09^s.86$, Dec = $+03°22'29''.3$, with an error radius of $2'.5$ (Mereghetti et al. 2007). At the time of the burst, Swift/BAT was pointing in almost the opposite direction and it would have been in the field of view two minutes later. The corresponding flux at the position of the burst, in a 300 s image beginning 130 s after the INTEGRAL trigger, is negligible.

The γ-ray prompt emission in the 20–200 keV energy band lasted about 50 s, with a peak flux of 0.9 ph cm^{-2} s^{-1} (1 s integration time) and a fluence of $(2 \div 3) \times 10^{-6}$ erg cm^{-2} (Mereghetti et al. 2007; Sazonov et al. 2007).

The Rapid Eye Mount[1] (REM; Zerbi et al. 2001) telescope reacted promptly and began observing 55 s after the GRB trigger time (see Sect. 3.1), discovering a bright fading IR counterpart within the INTEGRAL error circle at RA = $05^h50^m08^s.21$, Dec = $+03°22'30''.3$ (J2000; Covino et al. 2007), corresponding

---

[1] http://www.rem.inaf.it/

to Galactic coordinates (l, b) of $(202°766, −11°998)$. The afterglow was soon confirmed by PAIRITEL (Bloom 2007).

The Swift narrow field instruments, XRT and UVOT, began observing at 7004 s after the trigger time. The XRT found an uncatalogued fading source at the position RA = $05^h50^m08^s43$, Dec = $+03°22′30″0$ (J2000), with an error radius of $3″8$ and $3″3$ from the optical counterpart (Guidorzi et al. 2007). No optical source was detected corresponding to the optical and X-ray afterglows by UVOT down to $V = 19.5$ and $B = 20.5$ (3σ) from 197 s exposures (Holland et al. 2007).

The 2.2 m telescope of Calar Alto (CAHA) equipped with the Calar Alto Faint Object Spectrograph (CAFOS) observed the afterglow in the R filter at 0.72 and 1.73 days after the burst. Because of the low Galactic latitude, the Galactic reddening along the direction to the GRB is large: $E_{B−V} = 0.763$ mag (Schlegel et al. 1998). The Galactic extinction in each filter has been estimated through the NASA/IPAC Extragalactic Database extinction calculator[2]. Specifically, the extinction in the other filters is derived through the parametrisation by Cardelli et al. (1989): $A_V = 2.53$, $A_R = 2.04$, $A_I = 1.48$, $A_J = 0.69$, $A_H = 0.44$, $A_K = 0.28$ mag.

3. Data reduction and analysis

3.1. γ-ray data

Figure 1 shows the 18–200 keV background-subtracted time profile of GRB 070311 as recorded by INTEGRAL (Sazonov et al. 2007). The onset of the GRB appears to occur about 45 s before the trigger time. Hereafter, all times will be given relative to the onset time, i.e. 45 s prior to the trigger time. From 75 to ∼125 s the signal drops below the sensitivity of the instrument. Interestingly, between ∼125 and 225 s there is a hint of the presence of a faint γ-ray tail. Although this feature is detected at a ∼2.5-σ confidence level (see thick cross in Fig. 1), so should be regarded as tentatively detected, it is interesting to see how it fits into the overall picture together with near infrared (NIR), optical and X-ray observations of GRB 070311. We address this issue below.

The integrated spectrum in the 18–300 keV band is well fit by a power law with a photon index of $\Gamma_\gamma = 1.3 \pm 0.1$ and a fluence of $(3.0 \pm 0.5) \times 10^{-6}$ erg cm^{-2} (20−200 keV). The spectrum shows no statistically significant high-energy cut-off. The peak energy lies above 80 keV during the prompt emission. There is also an indication of spectral softening in the course of the burst, with Γ_γ evolving from 0.8 ± 0.2 during the rise phase to 1.45 ± 0.15 during the peak and decay of the emission (Sazonov et al. 2007). The conversion factor from rate to flux units in the 18−200 keV band is $(1.2 \pm 0.2) \times 10^{-9}$ erg cm^{-2} count^{-1}.

3.2. Infrared/optical data

Early time optical and NIR data were collected using the 60 cm robotic telescope REM located at the ESO La Silla observatory (Chile). The REM focal instruments consist of a NIR camera (REMIR), operating in the range 1.0−2.3 μm ($z′JHK′$), and an optical imager (REM Optical Slitless Spectrograph, ROSS) with spectroscopic (slitless) and photometric capabilities (VRI). A dichroic allows simultaneous observations at optical and NIR wavelengths in two selected filters (for further information on REM and its capabilities, see Covino et al. 2004, and references therein).
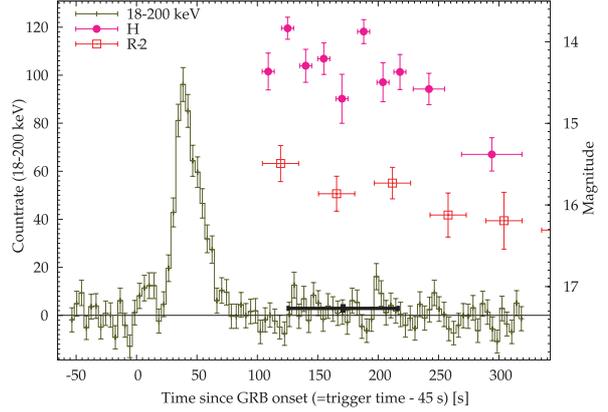
Fig. 1. Histogram of the INTEGRAL 18–200 keV background-subtracted γ-ray profile of GRB 070311 (integration time of 4 s; left axis). The thick cross shows a grouped bin of the γ-ray profile, ∼2.5σ above the background. REM H (filled circles) and R (empty squares) magnitudes of the NIR/optical afterglow are also reported on the right axis.

REM reacted promptly to the INTEGRAL GCN alert and began observing the field of GRB 070311 55 s after the burst trigger (36 s after the reception of the alert), following the event for ∼1 h.

For the first ∼500 s the REMIR observations were performed using only the H filter with increasing exposure times, then all the NIR filters were used in rotation. A similar observing strategy was adopted in the optical. R band observations lasted ∼1400 s for a total of 40 consecutive images. During the following ∼2700 s, VRI images were acquired in rotation but the optical transient was already below the instrument detection limits for the V and I filters.

For both optical and NIR data sets, the reduction and the analysis were performed following standard procedures. The photometric calibration for the NIR was accomplished by applying average magnitude shifts computed using the 2MASS[3] catalogue. The optical data were calibrated using instrumental zero points, checked with observations of standard stars in the SA95 Landolt field (Landolt 1992), or with the SDSS[4] in the case of the $z′$ filter.

Figure 1 shows the REM HR prompt measurements together with the γ-ray time profile, while Fig. 2 shows the $KHJz′R$ light curves.

Further observations were acquired with CAFOS. This instrument is a focal reducer, which allows direct imaging, spectroscopy and polarimetry. The detector used is a SITe 2048 × 2048 pixel CCD providing a scale of $0″53$ pixel^{-1} and a circular field of view of 16′ in diameter. In order to reduce the CCD read-out time, the observations of GRB 070311 were carried out by trimming the CCD to a 1024 × 1024 window. The photometric calibration was performed observing the standard field PG0942 (Landolt 1992) at a similar airmass as the GRB field. Data reduction and analysis were carried out following standard procedures by using ESO-Eclipse (v5.0) tools (Devillard 2001). Aperture photometry was obtained with the GAIA[5] (v3.2.0) package. REM and CAFOS photometry are reported in Table 1.
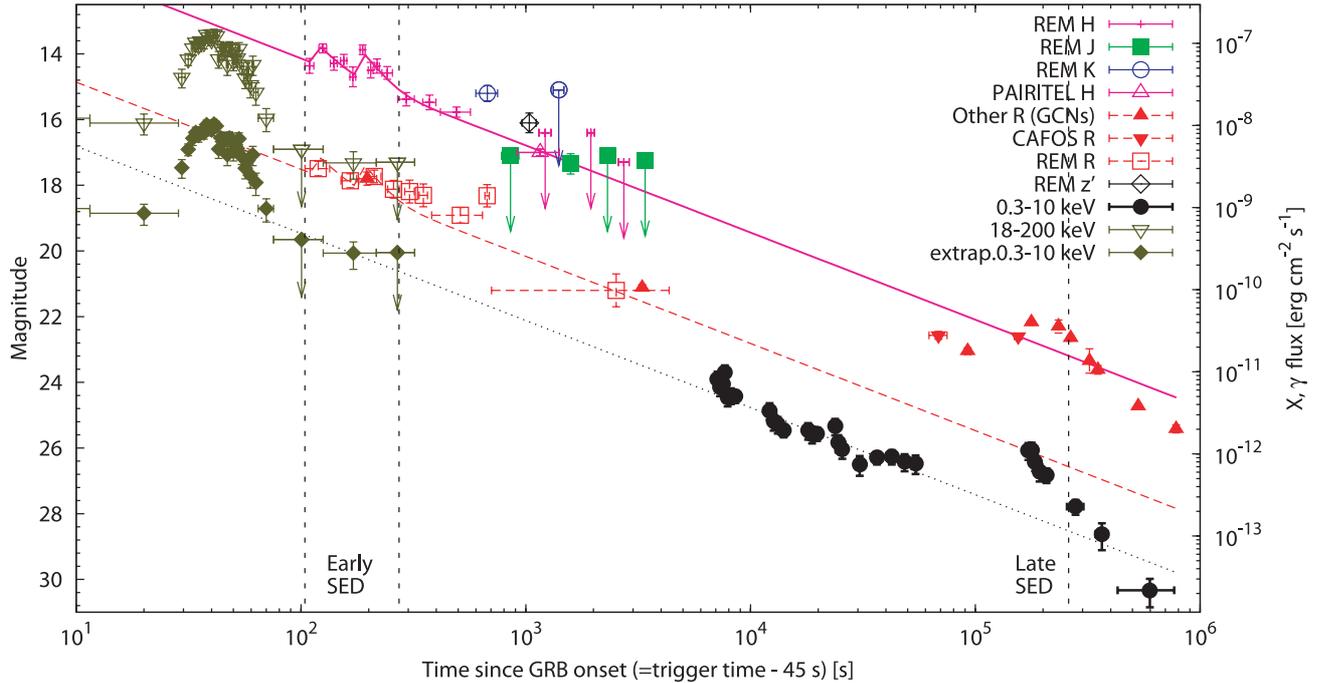
Hereafter, the magnitudes shown are not corrected for Galactic extinction, whilst fluxes and all the best-fit models are.

---

[2] http://nedwww.ipac.caltech.edu/forms/calculator.html

[3] http://www.ipac.caltech.edu/2mass/

[4] http://www.sdss.org

[5] http://star-www.dur.ac.uk/~pdraper/gaia/gaia.html

Fig. 2. Panchromatic light curves of the prompt and of the afterglow emission of GRB 070311: the flux in the $18-200$ keV band by INTEGRAL (empty upside down triangles) and in the $0.3-10$ keV band of the late afterglow by Swift/XRT (filled circles) are given on the right axis. Filled diamonds show the γ-ray flux extrapolated to the $0.3-10$ keV band. Magnitudes in J (filled squares), H (crosses), K (empty circles), z' (empty diamond) and R (empty squares) filters by REM and R by CAFOS (filled upside down triangles) are given on the left axis. A single H point from PAIRITEL (Bloom et al. 2007; empty triangle) and other R points from GCN circulars (Cenko 2007; Dai et al. 2007; Garnavich et al. 2007; Halpern & Armstrong 2007,b,c,d; Jelínek & Prouza 2007; Kann et al. 2007; Wren et al. 2007; filled triangles) are also shown. Upper limits are at 3-σ confidence level. The solid (dashed) line shows the best-fit power law ($\alpha = 1.06 \pm 0.08$) and two pulses superposed on the H (early R, i.e. $t < 10^4$ s) filter curve. The dotted line shows the same power-law component renormalised to the first part ($t < 10^5$ s) of the X-ray curve ($\alpha_x = \alpha_H = \alpha_R$). The two earliest vertical dashed lines show the time interval used to extract an early SED (Fig. 10), while the third vertical line shows the epoch of a late SED (Fig. 11).

When the models are plotted together with magnitudes, the correction for Galactic extinction is removed.

First we fitted the H light curve, which is the one best monitored at early times. We tried to fit the points up to $\sim$300 s with a simple power law to test whether the fluctuations visible in Fig. 1 are statistical variations around a power-law decay. The resulting χ^2/d.o.f. is 17.5/7 with a chance probability of 1.4% and a power-law index of $\alpha_H = 0.5 \pm 0.4$ (1σ). This probability becomes even smaller if the R and H points are combined. We infer that the probability that the first 300 s NIR/optical profile is the result of statistical fluctuations around a simple power-law decay is lower than 1.4%.

This motivated us to fit the early data by means of a more detailed model. The point from PAIRITEL at $t = 1160$ s (Bloom 2007) was included in the H data set for this analysis. The fit shown in Fig. 2 (solid line) is the result of a power-law component with decay index of $\alpha_H = 1.06 \pm 0.08$ with two FRED-shaped pulses superimposed, peaking at 119 and 180 s, respectively. The dashed line shows the power law fitting the early part of the R curve ($t < 10^4$ s) by fixing the index $\alpha_R = \alpha_H$ and allowing only the normalisation to vary. Here we note the less pronounced enhancement in the R flux at the time of the pulses seen in H. A more detailed discussion of this as well as of the fitting models, is reported in Sect. 4.1.

For both the K and J magnitudes there is one single detection and the remaining measurements are upper limits. The first J upper limit at 810 s, preceding the detection at 1537 s, is however inconsistent with the assumption $\alpha_J = \alpha_H$ extrapolated at the time of the two measurements. Comparing all the optical-NIR

filters, a flux increase characterised by some variability seems to appear even after the first two optical peaks, i.e. after $\sim$600 s. This, combined with the detections in J and z', could be a hint of a third flare.

3.3. X-ray data

The XRT began observing GRB 070311 on 2007 March 11 at 03:49:34 UT, 7004 s after the INTEGRAL trigger, and ended on 2007 March 19 at 22:38:54 UT, with a total net exposure of 81.8 ks in photon counting (PC) mode spread over 8.8 days. Table 2 reports the log of the XRT observations.

The XRT data were processed using the FTOOLS software package (v. 6.1) distributed within HEASOFT. We ran the task *xrtpipeline* (v.0.10.4) applying calibration and standard filtering and screening criteria. Data were acquired only in PC mode due to the faintness of the source. Events with grades $0-12$ were selected. The XRT analysis was performed in the $0.3-10$ keV energy band.

3.3.1. Temporal analysis

Source photons were extracted from a circular region with a 20 pixel radius (1 pixel = 2″36; Fig. 3) and point spread function (PSF)-renormalised. The background was estimated from a four-circle region with a total area of 11.5×10^3 pixel^2 away from any source present in the field. When the count rate dropped below $\sim 10^{-2}$ counts s^{-1}, we made use of XIMAGE with the tool

Table 2. XRT observation log of GRB 070311.

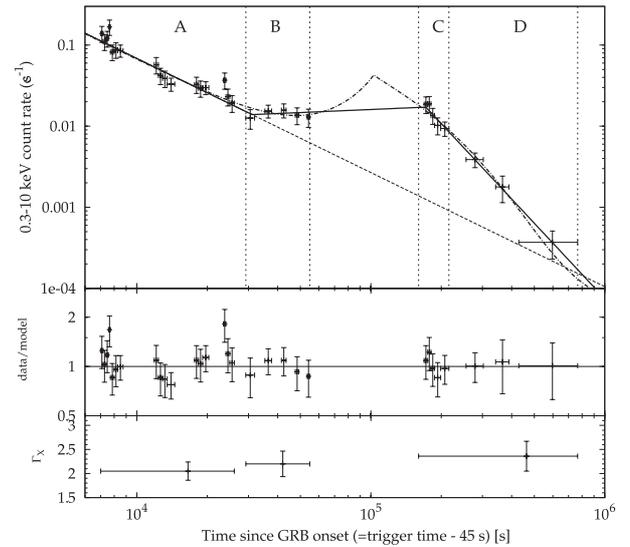| Sequence	Obs mode	Start time (UT)	End time (UT)	Exposure (s)	Start time[a] (s)	End time[a] (s)
00020052001	PC	2007-03-11 03:49:34	2007-03-11 17:08:03	18 780	7004	54 913
00020052002	PC	2007-03-13 00:49:40	2007-03-13 13:46:56	9697	169 010	215 646
00020052003	PC	2007-03-14 00:49:36	2007-03-14 13:53:56	9465	255 406	302 466
00020052004	PC	2007-03-15 00:47:36	2007-03-15 14:01:54	9954	341 686	389 344
00020052005	PC	2007-03-16 01:06:34	2007-03-16 23:41:55	9028	429 224	510 545
00020052006	PC	2007-03-17 01:08:59	2007-03-17 22:21:55	14 574	515 769	592 145
00020052007	PC	2007-03-17 23:45:20	2007-03-18 22:32:56	6283	597 150	679 206
00020052008	PC	2007-03-19 00:04:45	2007-03-19 22:38:54	3711	684 715	765 964

[a] Since INTEGRAL trigger time.
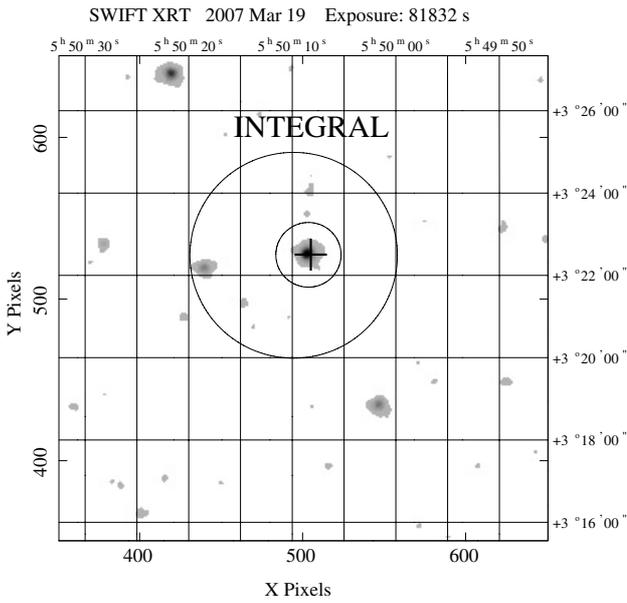
Fig. 3. XRT image of the field of GRB 070311 obtained from 82 ks PC data. The large circle shows the INTEGRAL position with an error radius of 2.5 (90% CL). The cross shows the optical afterglow position discovered by REM. The small circle is a 20 pixel radius region centred on the XRT afterglow.

Fig. 4. *Top panel*: X-ray afterglow light curve of GRB 070311 obtained with XRT in the 0.3–10 keV energy band. The solid line shows the best fit obtained with a double broken power law, while the dashed line shows the extrapolation of the initial power-law decay. The dashed-dotted line shows the best-fit combination of a FRED-like pulse superposed on a power law. Labelled vertical slices correspond to four different regions where spectra have been extracted. *Mid panel*: fractional residuals with respect to the double broken power-law model. *Bottom panel*: photon index (error bars are 1σ).

SOSTA, which corrects for vignetting, exposure variations and PSF losses within an optimised box, using the same background region.

The resulting 0.3–10 keV light curve is shown in Fig. 4. It was binned so as to achieve a minimum signal to noise ratio (SNR) of 3, except for the last two bins (with a SNR of 2.8 and 2.6, respectively), as well as a minimum of 20 total counts.

The light curve was fit firstly with a double broken power law (solid line in Fig. 4), whose best fit parameters are the following: $\alpha_{x,1} = 1.4 \pm 0.1$, $\alpha_{x,2} = -0.1^{+0.7}_{-0.2}$, $\alpha_{x,3} = 3.1^{+0.5}_{-0.4}$, $t_{x,b1} = 31 \pm 4$ ks, $t_{x,b2} = 1.7^{+0.1}_{-0.4} \times 10^5$ s (χ^2/d.o.f. $= 16.8/24$), where $\alpha_{x,i}$ ($i = 1, 2, 3$) are the canonical initial, mid, and final decay slopes and $t_{x,bi}$ ($i = 1, 2$) are the two break times, respectively. The last point lies on the extrapolation of the initial power-law decay (dashed line in Fig. 4). From the X-ray data alone it is not possible to determine whether the shallow and final steep decay phases are the result of a late rebrightening, after which the decay will resume to the pre-break behaviour.

We also adopted two alternative models: the combination of a FRED-shaped pulse with a power law (dash-dotted line in Fig. 4; a more detailed description follows in Sect. 4.1.2), and the model by Willingale et al. (2007). This model is the combination
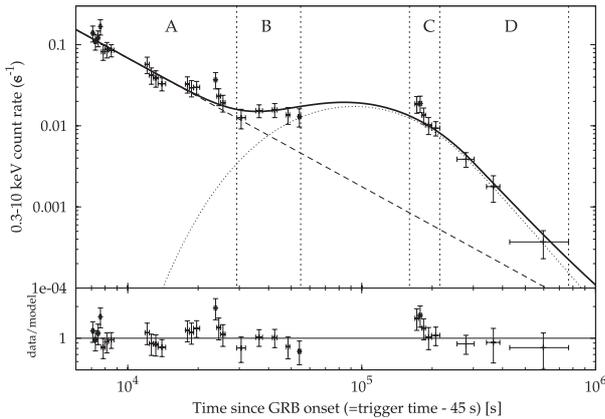
of two components, the prompt and the afterglow (according to the terminology introduced by these authors), described with the same functional form, which consists of a combination of an exponential and a power law. Following the notation by Willingale et al. (2007), we fixed the rise time of the prompt component to the onset time: $t_p = 0$. We also fixed the time when the power-law component of the prompt takes over, $T_p = 5 \times 10^3$ s, i.e. prior to the beginning of the X-ray observations, when the X-ray decay is already dominated by the power law. The best-fit model is shown in Fig. 5. The best-fit parameters are the following: $\alpha_p = 1.6 \pm 0.2$, $t_a = (1.0 \pm 0.4) \times 10^5$ s, $T_a = (2.9 \pm 1.0) \times 10^5$ s, $\alpha_a = 3.5 \pm 0.7$ (χ^2/d.o.f. $= 24.9/24$). We point out that within this model the late rebrightening corresponds to the onset of the afterglow component: this forced us to decouple t_a from T_p and treat the former as a free parameter, unlike what Willingale et al. (2007) did for all of the GRBs of their sample. The two-component model by Willingale et al. (2007) usually accounts for both the prompt and the afterglow emission. In our fit, we have only considered the late-time light curve. The X-ray rebrightening observed in GRB 070311 would therefore

Table 3. Best-fit parameters of the 0.3–10 keV spectrum of the X-ray afterglow. The model is an absorbed power law (xspec model: WABS POW).

Interval	Start time (s)	Stop time (s)	$N_{\rm H}$ (10^{21} cm^{-2})	$\Gamma_{\rm x}$	Mean flux (10^{-13} erg cm^{-2} s^{-1})	χ^2/d.o.f.
A	7004	26 079	$4.5^{+1.3}_{-1.0}$	$2.05^{+0.27}_{-0.24}$	24 ± 4	11.0/16
B	29 217	54 833	$4.2^{+3.2}_{-2.1}$	$2.2^{+0.6}_{-0.5}$	6.4 ± 1.9	351.5 (63.4%)[a]
C	160 010	215 648	$3.4^{+1.7}_{-1.4}$	$2.2^{+0.5}_{-0.4}$	5.6 ± 1.4	320.4 (58.2%)[a]
BC	29 217	215 648	$5.0^{+1.9}_{-1.9}$	$2.5^{+0.6}_{-0.5}$	4.5 ± 1.5	12.4/9
BCD	29 217	765 966	$5.5^{+2.1}_{-1.7}$	2.5 ± 0.2	1.9 ± 0.1	10.3/13
CD	160 010	765 966	$4.4^{+2.1}_{-1.3}$	2.4 ± 0.4	1.1 ± 0.4	6.2/7

[a] Cash statistics (C-stat; Cash 1979) and percentage of Monte Carlo realisations that had statistic <C-stat. We performed 10^4 simulations. Photons were extracted from a circular region with a 10 pixel radius.

Fig. 5. *Top panel*: X-ray afterglow light curve of GRB 070311 obtained with XRT in the 0.3–10 keV energy band. The curve has been fit with the two-component model by Willingale et al. (2007): the prompt (dashed), the afterglow (dotted) and their combination (solid). Labelled intervals are the same as in Fig. 4. *Bottom panel*: fractional residuals with respect to the model.

constitute a third component, which is only rarely seen in afterglow light curves.

3.3.2. Spectral analysis

In order to detect possible spectral variations connected with changes in the X-ray light curve, we extracted the 0.3–10 keV spectrum in four different time intervals, labelled "A", "B", "C" and "D", corresponding to the initial steep decay, the beginning of the shallow phase, the end of the shallow phase (or the peak of the rebrightening, according to the alternative description of the X-ray light curve discussed in Sect. 3.3.1), and the final steep decay, respectively (see Fig. 4).

Source and background spectra were extracted from the same regions as the ones used for the light curve (Sect. 3.3.1), except for intervals "B" and "C". For these intervals, due to their poor statistics, it was not possible to group the energy channels so as to have a Gaussian distribution of the number of photons per grouped channel. Hence, for both spectra we replaced the χ^2 with the C statistics (Cash 1979), which has proven to be useful whenever the Gaussian approximation does not hold (e.g. when the number of photons per bin is less than 10), provided that the contamination of background photons is negligible. In order to ensure this, for both spectra "B" and "C", a 10 pixel radius circular region was used.

The ancillary response files were generated using the task xrtmkarf. Spectral channels were grouped so as to have at least 20 counts per bin, except for "B" and "C". Spectral fitting was performed with xspec (v. 11.3.2). All the spectra can be modelled with an absorbed power law with the xspec models WABS POW. We assumed the photoelectric cross section by Morrison & McCammon (1983). Results of the best-fit parameters are reported in Table 3.

The Galactic neutral hydrogen column density along the GRB direction from 21 cm line radio surveys is $N_{\rm HI}^{\rm (Gal)} = 2.3 \times 10^{21}$ cm^{-2} (Kalberla et al. 2005). The X-ray absorption found from spectral fitting is significantly higher, by approximately two times, than $N_{\rm HI}^{\rm (Gal)}$. We do not interpret this as evidence for intrinsic absorption: for low Galactic latitudes ($b < 25°$) the $N_{\rm H}$ measured from X-rays is about twice as high as that derived from the radio, interpreted as being due to the presence of molecular gas (Arabadjis & Bregman 1999; Baumgartner & Mushotzky 2006). Therefore, we conclude that the $N_{\rm H}$ we measure from the X-ray spectrum is consistent with the Galactic value expected in the direction of GRB 070311, although we cannot exclude some intrinsic absorption.

Comparing the best-fit parameters obtained for the different spectra, while the absorption seems constant, we find the suggestion (2.2σ) for a softening of the photon index $\Gamma_{\rm x}$, from $2.05^{+0.27}_{-0.24}$ (interval A) to 2.5 ± 0.2 (intervals B, C, D merged together). The corresponding spectra with the best-fit models are shown in Fig. 6. We note that the change of the spectral index, $\Delta\beta_{\rm x} = \Delta\Gamma_{\rm x}$, is consistent with the canonical value of $1/2$ expected in the standard synchrotron model when the cooling frequency crosses the observed passband (X-rays, in this instance). In this case, this passage would have occurred approximately between intervals A and BCD (Fig. 4). The excess visible between 4 and 5 keV in the residuals of the spectrum with respect to the absorbed power law appears to be ~2.5σ significant in the most favourable case after rebinning (Fig. 6).

4. Multi-band combined analysis

4.1. Light curves fitting

We analysed the different decays in different energy bands as homogeneously as possible. Motivated by the possible interpretation of the FRED in the external shock context, and by the shape of the *H*-filter pulses similar to that of the prompt emission in the 18–200 keV band, which looks like a typical FRED, we first fitted the 18–200 keV pulse adopting the profile used by
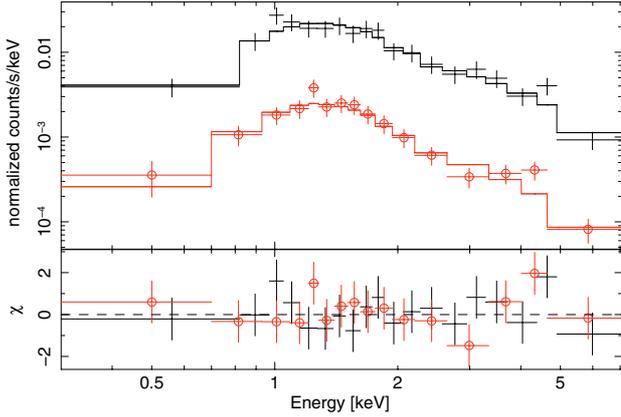
Fig. 6. *Top panel*: X-ray afterglow photon spectra of GRB 070311 obtained with XRT in the 0.3–10 keV energy band corresponding to the temporal interval A (crosses) and BCD (circles), respectively. Solid lines show the corresponding best-fit absorbed power laws. *Bottom panel*: residuals with respect to the corresponding best-fit models.

Norris et al. (1996):

$$F(t) = \begin{cases} A \ \exp\left[-\left(\dfrac{t_{max} - t}{\sigma_r}\right)^{\nu}\right], & t < t_{max} \\ A \ \exp\left[-\left(\dfrac{t - t_{max}}{\sigma_d}\right)^{\nu}\right], & t > t_{max} \end{cases} \quad (1)$$

where t_{max} is the peak time, σ_r and σ_d are the rise and decay times, respectively, A is the normalisation and ν is the peakedness (when $\nu = 1$ the profile is a simple exponential, when $\nu = 2$ it is a Gaussian). The best-fit parameters for the γ-ray pulse are: $t_{peak} = 39.0 \pm 0.8$ s, $\sigma_r = 8.5 \pm 1.0$ s, $\sigma_d = 15.0 \pm 1.7$ s. The peakedness was found to be $\nu = 1.08 \pm 0.13$, starting with an initial value of $\nu = 1$. The result is shown by the solid line in Fig. 7. We calculated the flux density at 88 keV, which corresponds to the energy at which the flux density equals the average flux density in the 18−200 keV band assuming $\beta_{\gamma} = 0.3$.

To fit the curves, we adopted two alternative approaches. First, we focused on the early pulses and fitted them in terms of two overlapping FRED-shaped pulses (PULSES model). We chose to model the shape of the pulses with a FRED, because this fits well, and also because it allows a better comparison with the results of the fit of the γ-ray pulse. Alternatively, we added a power-law continuum, in the assumption that the afterglow contribution is not negligible at this time (PL+PULSES model). Both H and R profiles were corrected for Galactic extinction. Given the less dense sampling of the H and R curve with respect to the γ-ray one, the peakedness was fixed to the best-fit value reported above.

Finally we fitted the late rebrightening seen in R and X-ray with a single pulse superposed to a power law (PL+PULSE model). Best-fit parameters of the models are reported in Table 4.

4.1.1. PULSES model

The first H pulse peaks 80 s after the γ-ray peak. The pulse shape is different: the rise time of the H pulse is about twice as long, while its decay time is about 4 times longer. The flux density normalisation constant, $A_{H1} = 4.9 \pm 0.3$ mJy, is about 17 times that of the γ rays at 88 keV. The second H pulse follows the first by ~62 s. Because of the poor sampling of the rise, only the decay is better constrained and turns out to be about twice as long as the decay time of the first pulse, while the normalisation of the second pulse is about half as big: $A_{H2} \simeq A_{H1}/2$, so that
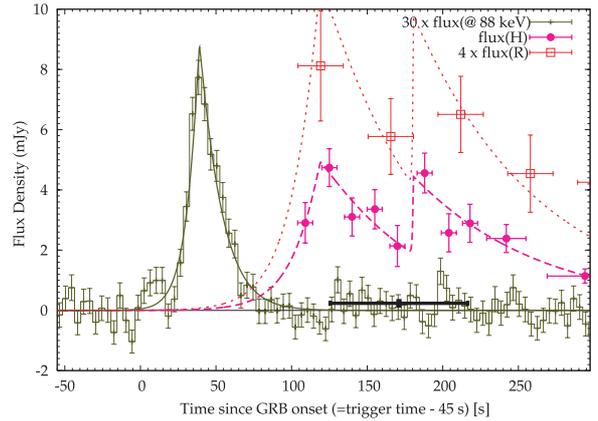
Fig. 7. INTEGRAL background-subtracted γ-ray flux density at 88 keV (crosses; integration time of 4 s) magnified 30 times, REM H (filled circles) and R (empty squares; magnified 4 times) flux densities of the NIR/optical afterglow (corrected for Galactic extinction). Solid, dashed and dotted lines show the best-fit models of the γ-ray, H- and R-band pulses, respectively. The thick cross is the same as that in Fig. 1.

the fluence during the decay is similar to that of the first pulse. The dashed line in Fig. 7 shows the sum of both pulses fitting the H points (filled circles).

To evaluate whether the R points simultaneous to the prominent pulses seen in H are consistent with being derived from the same profile as H within uncertainties, we integrated the best-fit model of the H curve over the R time bins. We determined the rescaling factor f_{best} that minimises the χ^2 between the measured R and the expected rescaled mean H flux. The result is shown in Fig. 8 and corresponds to $f_{best} = 0.55 \pm 0.06$, yielding χ^2/d.o.f. = 0.36/3. We conclude that the time profile best-fitting the H pulses is consistent with the simultaneous R measurements. R points and the best-fit model are displayed in Fig. 7, all magnified by a factor of 4 for the sake of clarity.

4.1.2. PL+PULSES model

In contrast to the description of Sect. 4.1.1, here we assume that the contribution of the power-law continuum is not negligible from the very beginning of the NIR/optical observations. The result is shown in Fig. 2. For the same reasons as in Sect. 4.1.1, we first fitted the H profile. The power-law continuum turned out to have a slope of $\alpha_H = 1.06 \pm 0.08$ (solid line in Fig. 2). We then added the same combination of pulses as that found in Sect. 4.1.1, by allowing the single normalisations and releasing gradually some of the parameters. Table 4 reports the best-fit values. Similarly to Sect. 4.1.1, the fit for the R filter was done by allowing just a scaling factor of the H profile. This turned out to be $f_{best} = 0.55 \pm 0.07$, i.e. the same as that obtained with the previous model (Sect. 4.1.1). The R best-fit profile is shown in Fig. 2 with a dashed line. The χ^2/d.o.f. of the best-fit model are acceptable: 6.0/7 and 12.1/8 for the H and R profiles, respectively.

The main differences from the results obtained in Sect. 4.1.1 concern the shorter rise times in this case, which were fixed to 0.1 s. This is a consequence of having increased the continuum component represented by the power law. The pulse shape is less constrained, for the same reason. The second pulse still has a longer decay than the first, while its peak intensity is now comparable with that of the first. The dotted line in Fig. 2 shows the best-fit power law of the X-ray data up to 10^5 s, obtained by fixing $\alpha_x = \alpha_H = \alpha_R$. The fit is acceptable: χ^2/d.o.f. = 24.3/21

Table 4. Best-fit parameters of the multi-band light curves of the afterglow of GRB 070311. Uncertainties are 1σ. Values of frozen parameters are reported among square brackets.

Energy band/filter	Model	Component	α	t_{peak}^{a} (s)	σ_{r} (s)	σ_{d} (s)	A (mJy)	ν
18–200 keV	PULSES	pulse	–	39.0 ± 0.8	8.5 ± 1.0	15.0 ± 1.7	0.29 ± 0.05^{b}	1.08 ± 0.13
H	PULSES	1st pulse	–	119.0 ± 2.2	18.2 ± 4.8	63.6 ± 5.2	4.9 ± 0.3	[1.08]
H	PULSES	2nd pulse	–	180.5 ± 9.4	0.5 ± 3.6	110 ± 15	2.6 ± 0.2	[1.08]
R	PULSES	1st pulse	–	[119.0]	[18.2]	[63.6]	2.7 ± 0.2	[1.08]
R	PULSES	2nd pulse	–	[180.5]	[0.5]	[110]	1.4 ± 0.1	[1.08]
H	PL+PULSES	pl	1.06 ± 0.08	–	–	–	3.6 ± 2.0^{c}	–
H	PL+PULSES	1st pulse	–	119.0 ± 0.1	[0.1]	27 ± 18	2.2 ± 1.0	[1.08]
H	PL+PULSES	2nd pulse	–	181.1 ± 0.6	[0.1]	41 ± 17	2.6 ± 0.8	[1.08]
R	PL+PULSES	pl	[1.06]	–	–	–	2.0 ± 1.1^{c}	–
R	PL+PULSES	1st pulse	–	[119.0]	[0.1]	[27]	1.2 ± 0.6	[1.08]
R	PL+PULSES	2nd pulse	–	[181.1]	[0.1]	[41]	1.4 ± 0.4	[1.08]
late R	PL+PULSE	pl	[1.06]	–	–	–	$11.0 \pm 0.9^{d,e}$	–
late R	PL+PULSE	pulse	–	19.1 ± 0.3^{f}	2.85 ± 0.54^{f}	7.4 ± 0.7^{f}	36 ± 4^{e}	0.91 ± 0.34
0.3–10 keV	PL+PULSE	pl	1.47 ± 0.20	–	–	–	$1.3 \pm 0.1^{d,g}$	–
0.3–10 keV	PL+PULSE	pulse	–	10 ± 3^{f}	2.9 ± 2.5^{f}	6.6 ± 0.9^{f}	24 ± 12^{g}	0.89 ± 0.56

[a] Time since GRB onset (corresponding to 45 s before the trigger time). [b] Flux density corresponding at 88 keV. [c] Flux at $t = 100$ s. [d] Flux at $t = 10^5$ s. [e] Units of μJy. [f] Units of 10^4 s. [g] Units of 10^{-13} erg cm^{-2} s^{-1}.
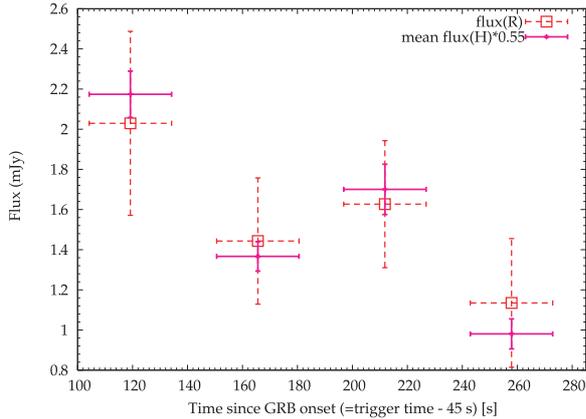
Fig. 8. Early R optical flux (dashed squares) compared with the time-integrated flux expected from the best-fit model of the H curve rescaled by a factor of 0.55 ± 0.06, which minimises the χ^2.

(chance probability of 28%). This description of the X-ray light curve is different from that given in Sect. 3.3.1.

We tentatively extrapolated the γ-ray flux to the 0.3–10 keV band, assuming the simple power law with $\Gamma_\gamma = 1.3 \pm 0.1$ (Sect. 3.1). This assumption relies upon the fact that the peak energy is likely to lie above 80 keV because of the hardness of the photon index Γ_γ. We also applied the suppression factor due to the soft X-ray absorption measured in the X-ray spectrum. The result is shown in Fig. 2. Interestingly, the single power law derived from fitting the early H and R continuum components, $\alpha_x = 1.06$, matches the level of the extrapolated prompt emission flux in the X-ray band.

4.1.3. Late R/X-ray rebrightening

From Fig. 2 we note that the power-law continuum, over which the late ($t \sim 2 \times 10^5$ s) R rebrightening sets in, looks brighter than expected from extrapolating the early best-fit model by

~1 order of magnitude. For this reason we fitted it separately from the early R light curve. We adopted a combination of a power-law and a single pulse (Eq. (1)). The power-law index was fixed to the value found in Sect. 4.1.2 for the early part of the R, i.e. $\alpha_R = 1.06$. The result is shown in Fig. 9 (thick dashed line). We did the same for the contemporaneous 0.3−10 keV profile (thick solid line in Fig. 9). We initially fixed $\alpha_x = \alpha_R$ in analogy with Sect. 4.1.2, but we had to release it because of the badness of the fit and it turned out to be $\alpha_x = 1.47 \pm 0.20$, more consistent with the broken-power-law fit given in Sect. 3.3.1. The X-ray coverage of the late rebrightening is not as detailed in catching the peak time as for the R filter, nonetheless from Fig. 9 we can confidently affirm that X-rays peak earlier than optical, which is rising or flattening during the beginning of the monitored X-ray decay. Best-fit parameters are reported at the bottom of Table 4.

The dashed-dotted line in Fig. 9 represents the case when the X-ray late rebrightening is fit with the sum of two power laws, the second of which turns on between 6×10^4 and 2×10^5 s and models the rebrightening superposed to the first power law. The best-fit indices are $\alpha_{x,1}^{(pp)} = 1.4 \pm 0.1$ and $\alpha_{x,2}^{(pp)} = 3.5 \pm 0.5$, respectively ($1\sigma$ confidence). For both components, the time origin was fixed to the GRB onset time. The time at which the second power law sets in cannot be estimated from our data, however, this is irrelevant for determining the power-law indices.

Compared to the R band, the poorer coverage of the X-ray peak reflects upon bigger uncertainties on the best-fit parameters of the X-ray profile. Interestingly, rise and decay times are similar and the ratios $\sigma_{\mathrm{d}}/\sigma_{\mathrm{r}}$ are 2.3 and 2.6 for the R filter and X-ray, respectively, i.e. the pulses resemble the typical shape of a prompt γ-ray pulse (Norris et al. 1996). The peak intensities are 6.5 ± 0.9 and 18 ± 9 times the value of the correspondent underlying power-law at peak time for the R filter and X-ray band, respectively. The X-ray/R time lag amounts to $(9.1 \pm 3.3) \times 10^4$ s. More simply, the late R rebrightening peaks twice as late as the X-ray profile. A word of caution is needed regarding the evaluation of this temporal lag: the uncertainty could be larger than our estimate, which is constrained by the choice of the functional
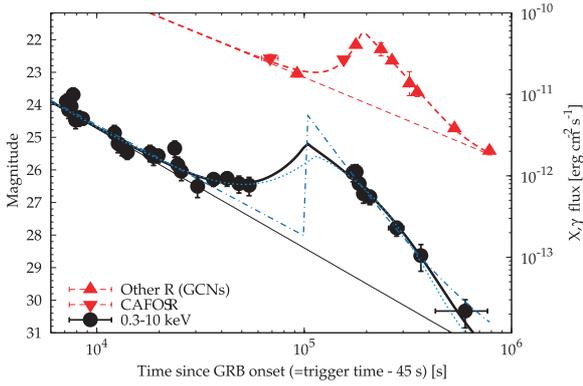
Fig. 9. Late time rebrightening and correspondent best-fit models (power law and a pulse) seen in R filter (triangles, thick dashed line) and 0.3–10 keV band (circles, thick solid line). Thin lines show the correspondent power-law component alone. X-rays: the dotted line shows the rescaled version of the γ-ray prompt pulse combined with the underlying power law, while the dashed-dotted line represents the sum of two power laws.

form used for fitting. Nevertheless, the evidence for a positive lag is apparent, regardless of the fits.

4.1.4. Prompt γ pulse/late X-ray rebrightening

Notably, the ratios between the temporal parameters best fitting the pulse of the γ-ray prompt profile (Sect. 4.1.1), and their corresponding ones fitting the late X-ray rebrightening (Sect. 4.1.3), are all comparable: $t_{\mathrm{peak,lateX}}/t_{\mathrm{peak},\gamma} = 2600 \pm 800$, $\sigma_{\mathrm{r,lateX}}/\sigma_{\mathrm{r},\gamma} = 3400 \pm 3000$, $\sigma_{\mathrm{d,lateX}}/\sigma_{\mathrm{d},\gamma} = 4400 \pm 800$. We tried to fit the late X-ray rebrightening with the combination of the same power law as that obtained in Sect. 4.1.3 and a rescaled version of the γ-ray prompt pulse: $t_{\mathrm{peak,lateX}} = f_{\mathrm{s,X}}(t_{\mathrm{peak},\gamma} - t_0)$, $\sigma_{\mathrm{r,lateX}} = f_{\mathrm{s,X}}\,\sigma_{\mathrm{r},\gamma}$, $\sigma_{\mathrm{d,lateX}} = f_{\mathrm{s,X}}\,\sigma_{\mathrm{d},\gamma}$. We left three parameters free to vary: the scaling factor $f_{\mathrm{s,X}}$, the time origin t_0 and the normalisation of the pulse. The choice of letting the time origin vary was motivated by the peak time of the γ-ray pulse being very sensitive due to its smallness. The result is shown in Fig. 9 (dotted line). The best-fit parameters are the following: $f_{\mathrm{s,X}} = 5700 \pm 700$ and $t_0 = -19.0 \pm 2.4$ s ($\chi^2/\mathrm{d.o.f.} = 19.3/27$). The potentially strong implications on the interpretation of this result are addressed in Sect. 5.

4.2. Spectral energy distribution evolution

We derived two spectral energy distributions (SEDs) at different epochs. The early one comprises the NIR pulses seen at the beginning of the REM follow-up observations and lasts from 104 to 273 s. This SED consists of detections in two filters, H and R, and a 3-σ upper limit of 6.3 μJy in the 18–200 keV band (see Fig. 2). Given the high variability of the H curve, especially when compared with that of R, the mean H flux was derived by integrating the best-fit profile of the H curve described in Sect. 4.1.1 over this time interval. The simultaneous mean R flux was calculated assuming the best-fit rescaling factor ($f_{\mathrm{best}} = 0.55 \pm 0.06$) between H and R derived in Sect. 4.1 for the same time interval. The fit with a simple power law yields $\beta_{\mathrm{NIR-opt}} = 0.65 \pm 0.21$. The extrapolation of the fit to the γ-ray band is consistent with the upper limit (Fig. 10).

Interestingly, the spectral index is consistent with that at the end of the γ-ray pulse (Sect. 3.1), $\beta_{\gamma} = 0.45 \pm 0.15$, and might be suggestive of an unbroken power law segment from NIR to
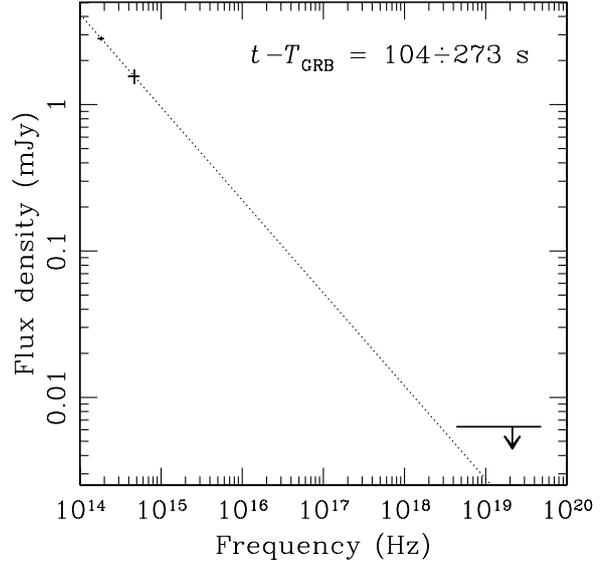

Fig. 10. NIR-optical/γ-ray SED between 104 and 273 s after the GRB onset time. The dotted line shows the best-fit power law, with $\beta_{\mathrm{NIR-opt}} = 0.65 \pm 0.21$. The upper limit is at 3σ.

γ at this epoch. However, the large value of E_{B-V} makes the uncertainty δA_V on the Galactic extinction quite large, $\delta A_V \geq 0.5$ mag. Should the Galactic extinction in V be larger (smaller) by 0.5, the corrected spectral index of the NIR/optical data alone would be $\beta_{\mathrm{NIR-opt}} = 0.3 \pm 0.2$ ($\beta_{\mathrm{NIR-opt}} = 1.0 \pm 0.2$). Thus, nothing conclusive can be said about the possible presence of extinction in excess of the Galactic one.

The late SED (Fig. 11) was extracted at 2.6×10^5 s, corresponding to the beginning of the decay following the late rebrightening in R simultaneously with the final steep X-ray decay (see Fig. 2). This SED includes a single R measurement taken by Halpern & Armstrong (2007) and the XRT spectrum BCD (Sect. 3.3.2; Table 3) renormalised through the best-fit power-law segment of the X-ray light curve (Sect. 3.3.1) at the epoch of the R point. The SED was fit with an SMC-extinguished (Pei 1992; in the observer frame), X-ray photoelectrically absorbed broken power law with $\beta_{\mathrm{x}} - \beta_{\mathrm{NIR-opt}} = 0.5$. The N_{H} was fixed to the value already derived from the corresponding X-ray spectrum, i.e. 5.5×10^{21} cm^{-2}, consistent with being entirely Galactic (Sect. 3.3.2). We found $\beta_{\mathrm{NIR-opt}} = 1.0 \pm 0.2$, consistent with $\beta_{\mathrm{x}} = 1.5$ from the X-ray spectrum best fit (Table 3). The break frequency turned out to be $\nu_{\mathrm{b}} = (3.0 \pm 0.9) \times 10^{17}$ Hz and $A_V = 0.80 \pm 0.15$ mag ($\chi^2/\mathrm{d.o.f.} = 9.6/12$). Figure 11 shows the SED: the dashed (dotted) line represents the best-fit model with optical extinction and X-ray absorption taken out (shown).

Alternatively, we tried to fit the SED with a single absorbed power law. If we leave the slope free to vary, the fit is driven by the more numerous X-ray points, leading to $\beta \sim 1.5$ and $A_V = 6 \pm 3$ mag. However, if we correct the early SED for such an extinction, the intrinsic optical spectrum would be nonphysically blue ($\beta_{\mathrm{opt}} = -3$). Otherwise, if we impose a single power law between optical and X-ray and fix $\beta_{\mathrm{opt-x}} = 1.0$, A_V becomes comparable with that found in the case of a broken power law. However, although the fit cannot be rejected ($\chi^2/\mathrm{d.o.f.} = 18/13$), the residuals of the X-ray points with respect to the model show a trend. Therefore, a simple absorbed power law does not seem to be a good representation of our data.

Because of the unknown redshift z of GRB 070311, we caution that the values of A_V computed in the fits above are
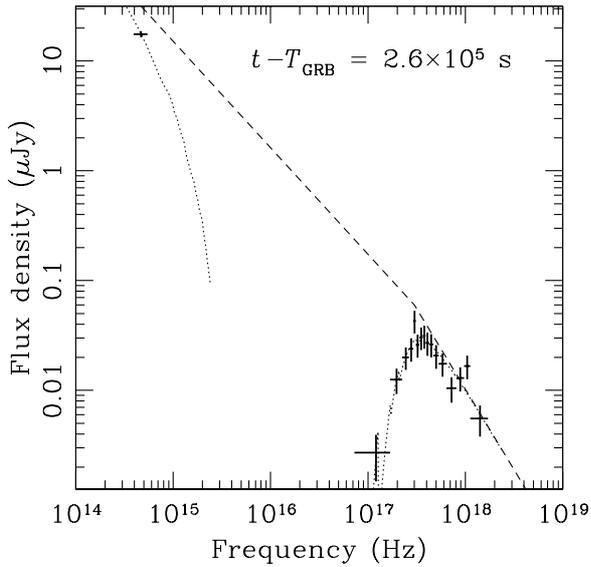
Fig. 11. Optical/X-ray SED at 2.6×10^5 s, around the peak of the late rebrightening. The dashed (dotted) line shows the best-fit absorbed broken power law, corrected (not corrected) for the optical extinction and X-ray absorption. The N_H was fixed to 5.5×10^{21} cm^{-2} found from fitting the X-ray spectrum alone, while A_V was found to be 0.80 ± 0.15 mag, adopting an SMC profile (at $z = 0$).

calculated for $z = 0$ assuming a specific extinction law (SMC model), so they must be taken as indicative upper limits to the corresponding rest-frame values. Unlike for the early SED, the X-ray absorption in terms of N_H is known to be consistent with the expected Galactic value. Due to the unknown redshift, it is not possible to set an upper limit to the possible intrinsic rest-frame $N_{H,z}$ absorption. For this reason, and because of the upper limits on A_V, nothing can be inferred on the amount of dust and gas along the line of sight to the GRB progenitor.

5. Discussion

Together with the early optical/NIR flares possibly accompanied by a γ-ray tail, the late, bright and long rebrightening seen in X-ray and R band probably is the most intriguing feature of GRB 070311. Although such late brightenings or flares are not unprecedented, only a few bursts have exhibited them so far: e.g. GRB 970508 (Piro et al. 1998; Galama et al. 1998), the short GRB 050724 (Campana et al. 2006; Malesani et al. 2007), the $z = 6.3$ GRB 050904 (Cusumano et al. 2007; Watson et al. 2006). We also note the presence of the shallow decay phase preceding the X-ray brightening (or corresponding to its gradual onset). Due to the lack of contemporaneous coverage in the R band, we did not observe a similar shallow decay phase in the optical bands. However, from Fig. 2 we infer that it must have taken place (e.g. some energy injection between $\sim 10^4$ s and $\sim 10^5$ s) to power the continuum component of the R-filter decay at late times, which is significantly above the extrapolation of the early data.

In the case of GRB 070311, we note that $\Delta t/t \sim 1$ for the late rebrightening in both X-ray and R filter, so timescales arguments cannot be used against an ES origin for it. This is in contrast to what has been observed for other GRBs (e.g. GRB 050502B, Burrows et al. 2005; Falcone et al. 2006; GRB 050724, Barthelmy et al. 2005; Campana et al. 2006), in which the rise and decay of the flares are too steep and require a resetting of the time origin.

In addition, the FRED-like shape of the 18–200 keV prompt light curve and consequent lack of high variability, classically used to argue against an external origin of the prompt emission of complex bursts (Sari & Piran 1997; but see also Dermer & Mitman 1999), indicates that the prompt emission of GRB 070311 is potentially consistent with it (e.g., see Kumar & Panaitescu 2003), although unlikely due to synchrotron radiation (Ramirez-Ruiz & Granot 2006).

Motivated by this and by the analogies found between prompt and late afterglow, hereafter we try to interpret the observations of GRB 070311 in the light of an external shock origin. While the γ-ray pulse is thought to be produced during the deceleration of the shell against the surrounding medium, we consider two alternative explanations for the late rebrightening: either a refreshed shock by a second shell emitted after the first one, or a single shell whose forward shock encounters a density bump.

The description of the R and X-ray late rebrightening as a simple power law with a slope changing after the peak (Sect. 4.1.3), is consistent with the interpretation that the late rebrightening is due to a thin shell that caught up with the shock front of the blastwave at later times, as expected in the so-called refreshed-shock scenario (Rees & Mészáros 1998). In this picture, the fireball rebrightened and soon afterwards ($\sim 2 \times 10^5$ s) turned off: the decay is the result of two components: the pre-existing power law and the high-latitude radiation left over by the refreshed shock. This is the case when the energy of the impacting shell is lower than that of the fireball (as also suggested by the ratio between the radiated energy during the late flare and the prompt emission), so that no noticeable step in the power-law decay is observed, but it is still luminous enough to produce a peak on a short timescale.

According to the so-called "curvature" effect (Fenimore et al. 1996; Kumar & Panaitescu 2000; Dermer 2004), the steepness of the fast decay phase of several X-ray afterglows, as well as of the γ-ray tail of single pulses, is due to high-latitude radiation Doppler-boosted in the observer fixed energy band. A relation is expected between temporal and spectral index: $\alpha = \beta + 2$ in its simplest form in the case of a thin shell emitting for a short time, where the time origin must correspond to the time of the GRB explosion as measured in the detector frame.

Notably, for GRB 070311 both the decay of the γ-ray pulse and the longer decays in X-rays and R-filter of the late rebrightening are consistent with the high-latitude closure relation and *with the same time origin*, i.e. the GRB onset time: $\alpha_\gamma \sim \beta_\gamma + 2 = 2.3 \pm 0.1$ and $\alpha_x = \beta_x + 2 = 3.5 \pm 0.2$. This is proven by the measured slope of the second power law, $\alpha_{x,2}^{(pp)} = 3.5 \pm 0.5$, which describes the flare decay, in addition to the underlying power law with $\alpha_{x,1}^{(pp)} = 1.4 \pm 0.1$ (Sect. 4.1.3). Therefore, if we adopt the combination of a power law and either a pulse or another power law for the late rebrightening (Sect. 4.1.3), the slope of the pulse decay is still consistent with a curvature effect: $\alpha_{x,2}^{(pp)} = \beta_x + 2$. In addition, from Sect. 4.1.4 we know that if we move the reference time backwards to 19.0 ± 2.4 s before the GRB onset, the late brightening is well fit by a time-rescaled version of the prompt γ-ray pulse. What is remarkable is that the peak time scales exactly in the same way as the pulse rise and decay times: $\Delta t_{\gamma,\text{prompt}}/t_{\gamma,\text{prompt}} = \Delta t_{x,\text{late}}/t_{x,\text{late}}$. This suggests that either two shells generated the prompt pulse as well as the late rebrightening or, alternatively, that a unique shell caused both by encountering two density enhancements. We note that the late X-ray hump occurs later (few $\times 10^4$ s) than what is more commonly seen in the typical flat phase ($\sim 10^3$ s),

also usually interpreted in terms of energy injection from the central engine. The detection in the R filter rules out a very high redshift, so such a late refreshing may be either due to a more distant radius of emission of the forward shock (e.g. due to low density of the surrounding medium) or due to a slow shell catching up with the shock front.

The 18–200 keV fluence emitted in the prompt amounts to $(3.0 \pm 0.5) \times 10^{-6}$ erg cm^{-2} by integrating the best-fit model of Sect. 4.1.1, while the net 0.3–10 keV fluence of the late rebrightening is $(2.4 \pm 1.2) \times 10^{-7}$ erg cm^{-2}, i.e. lower by one order of magnitude. If we extrapolate the prompt spectrum to the XRT band as in Sect. 4.1.2 and correct for the X-ray absorption, the fluence of the late X-ray rebrightening becomes comparable with that of the prompt extrapolated to the same energy band. Differently, the late R hump has a time-integrated flux about one order of magnitude larger than the early pulses seen in the same filter. The larger energy content of the late shock, with respect to the early one seen in optical, might be explained with an increasing efficiency in converting the kinetic energy of the blastwave into radiation. This implies a change of the microphysical parameters of the afterglow, as suggested to explain the shallow decay phase of other GRBs (Ioka et al. 2006; Panaitescu 2006). This can also be explained more simply as being due to the fact that the νF_ν broadband spectrum peaks at lower energies at later times, so that the energy release in the observed R filter during the late rebrightening is larger than during the prompt or soon after that.

Following Ioka et al. (2005), we can find which scenarios may be compatible with the observed flux increase, $\Delta F/F \approx 10$ (both in R and X; Sect. 4.1.3), and the observed $\Delta t/t \approx 1$: from their Fig. 1, the late hump of GRB 070311 is compatible with the refreshed shock scenario. Also the patchy shell model (Mészáros et al. 1998), characterised by an anisotropic emitting surface of the fireball, is not ruled out, while the scenario of a density bump causing the late rebrightening is ruled out, unless many clumps of matter are illuminated at the same time. Therefore, the bright flux of the rebrightening, $\Delta F/F \approx 10$, seems to disfavour the interpretation of a density medium enhancement, causing the observed flux increase. However we note that this is debated: e.g. according to Dermer & Mitman (1999) and Dermer (2007a), this could be produced by parts of the blastwave in which most of the energy has not been converted into radiation, yet, while impacting on a dense and thick clump of matter. In this scenario, the same shell would be responsible for both the prompt and the late rebrightening: e.g. the high-latitude emission observed during the decay of the late hump might be the result of the blastwave finally reaching the wind-termination shock. However, the interpretation of the late rebrightening being due to a density bump seems disfavoured by the crossing of the X-ray band by the cooling break ν_c, whereas the observed frequency must be below ν_c. In addition to that, the remarkable flux enhancement observed, $\Delta F_x/F_x = 18 \pm 9$ (Sect. 4.1.3), makes this interpretation less probable. In both scenarios (refreshed shock produced by another shell or density bump), the scaling factor of the timescale of the late brightening with respect to the early pulse, $f_s = 5700 \pm 700$, could result from the interplay of two factors: the increase of the visible portion of the emitting surface and the fact that the blastwave Lorentz factor has decreased by a factor of Γ_1/Γ_2 head on, thus stretching the timescale by $(\Gamma_1/\Gamma_2)^2$. Therefore, since $R_1 < R_2$, from $f_s = R_2/R_1 (\Gamma_1/\Gamma_2)^2$, it must be $\Gamma_1/\Gamma_2 < \sqrt{f_s} = 75 \pm 5$.

The early NIR/optical pulses detected soon after the γ-ray pulse are consistent with both interpretations: they could be the result of density bumps swept up by the blastwave

($\nu_{\rm NIR/opt} < \nu_c$), or other shells emitted soon after the first one and catching up with the shock front 80 and 140 s after its deceleration (Sect. 5.1).

During the late rebrightening, we know that the spectrum is likely described by a broken power law with $\beta_x = 1.5 \pm 0.2$ and $\beta_{\rm opt} = 1.0 \pm 0.2$. If we interpret it as the cooling break in the slow cooling regime, the electron power-law distribution index is $p = 3.0 \pm 0.4$. The fact that β_x was around 1.0 at the beginning of the XRT observations can be explained if the cooling frequency crossed the X-ray band during the observations. The change in the X-ray decay that would be implied amounts to 1/4 and could be still compatible with the pre-break slope, ranging from 1.0 to 1.4, depending on which model one assumes (Sects. 3.3.1, 4.1.2, 4.1.3). The optical decay $\alpha_R = 1.06 \pm 0.08$ is compatible with that expected in the case of an ISM environment: $\alpha_R^{\rm ISM} = 3(p-1)/4 = 1.5 \pm 0.3$. Differently, the case of a wind environment is ruled out (3σ): $\alpha_R^{\rm wind} = (3p-1)/4 = 2.0 \pm 0.3$.

Alternatively, if during the late rebrightening the bulk Lorentz factor has already decreased to $\Gamma < 1/\theta_j$, where θ_j is the jet opening angle, the afterglow should already have experienced an achromatic jet break: in this case, both optical and X-ray decay indices are simply equal to p. Notably, this is compatible with the measured values during the decay of the late rebrightening and this led Panaitescu (2007) to favour the jet interpretation for this burst. However, we believe that the late rebrightening is more likely to be due to an energisation of the blastwave shock front that strongly affected the measured power-law slope, similarly to what was inferred in the case of GRB 050724 (Malesani et al. 2007).

The interpretation of the final steep decay following the flare as the post jet-break decay seems unlikely: while the late X-ray flare might still be interpreted as a shallow-steep transition (Sect. 3.3.1), in the optical the identification as a flare cannot be questioned. Therefore, the steep decay after the peak simply corresponds to the declining part of the flare and not to a jet break.

5.1. Deceleration radius of the fireball

The result of Sect. 4.1.4 suggests that the time origin, moved to 19.0 ± 2.4 s before the GRB onset, would correspond to the explosion time in the detector frame (hereafter DF), i.e. when the shell radii are negligible. Let $t_{\rm expl} = -19.0$ s be the explosion time measured in the DF. In this context we can derive some clues on the fireball evolution produced during the first shock corresponding to the γ-ray pulse. In this picture the shell would expand from $t_{\rm expl}$ to $t_\gamma = 0$, when it would start emitting γ-rays. The deceleration time $t_{\rm dec}$ would correspond to the peak time of the γ-ray pulse, i.e. 39.0 ± 0.8 s. First the shell accelerates until it reaches the coasting radius (typically $\sim 10^{13}$ cm), while the bulk Lorentz factor increases linearly with radius until it reaches the maximum value of Γ_0. At this stage, the internal energy of the fireball has been converted into bulk kinetic energy. After that, the shell expands with constant $\Gamma = \Gamma_0$ until it is decelerated by the surrounding medium. If the time it takes the shell to reach the coasting phase is negligible with respect to the time it takes to begin to decelerate, it follows that during most of the time from $t_{\rm expl}$ to t_γ the shell was moving with Γ_0. In this case the shell would start decelerating at the radius $2 c (t_\gamma - t_{\rm expl}) \Gamma_0^2/(1+z) = 1.1 \times 10^{16} (\Gamma_0/100)^2 (1+z)^{-1}$ cm. The deceleration process would culminate at the deceleration radius $r_{\rm dec} = (3 E_{\rm iso}/4\pi n m_{\rm p} c^2 \Gamma_0^2)^{1/3} \simeq (5.4 \times 10^{16} \text{ cm})$ $(E_{\rm iso,52}/n)^{1/3} (\Gamma_0/100)^{-2/3}$ at the deceleration time (DF) $t_{\rm dec} = 94 (E_{\rm iso,52}/n)^{1/3} (\Gamma_0/100)^{-8/3} (1+z)$ s in the thin shell case

ploughing into uniform ISM (Rees & Mészáros 1992). We note that from the beginning to the peak of the deceleration, i.e. from t_γ to t_{dec}, the bulk Lorentz factor decreases approximately from Γ_0 to $\Gamma_0/2$. From this we can infer the distance travelled by the fireball in the same time interval: this must be between $2\,c\,(t_{\text{dec}} - t_\gamma)\,(\Gamma_0/2)^2/(1 + z)$ and $2\,c\,(t_{\text{dec}} - t_\gamma)\,\Gamma_0^2/(1 + z)$, i.e. between $0.6 \times 10^{16}\,(\Gamma_0/100)^2\,(1 + z)^{-1}$ cm and $2.3 \times 10^{16}\,(\Gamma_0/100)^2\,(1 + z)^{-1}$ cm. This is comparable with the distance already travelled at the beginning of the deceleration and consistent with the numbers reported above. The unknown redshift z unfortunately makes it too tentative to push these estimates any further.

6. Conclusions

GRB 070311 is a FRED-shaped burst followed by early NIR/optical pulses detected from ~100 to ~200 s and possibly accompanied by a simultaneous faint γ-ray tail, with subsequent variability detected at different NIR/optical filters up to ~10^3 s from the GRB onset. Another remarkable property exhibited by GRB 070311 is the late R and X-ray rebrightening observed around few 10^5 s after the burst, with the X-ray peaking earlier than R-filter photons. When we fit it with the combination of an underlying power law plus a pulse, the X-ray (R) fluence of the pulse alone is comparable (10 times larger) with that of the early pulse, while the peak intensity is about one order of magnitude larger than that of the underlying power law. Interestingly, if we refer the times to 19.0 ± 2.4 s prior to the GRB onset, it turns out that the peak time as well as the rise and decay times of the late pulse are compatible with the corresponding times of the γ-ray pulse, rescaled by the same factor: $f_s = 5700 \pm 700$. We interpreted this in the ES scenario, where the γ-ray prompt emission would correspond to the deceleration of the blastwave sweeping up the surrounding medium with uniform density, while the late R and X-ray rebrightening would be produced by the refreshed shock of another shell emitted after the first and impacting the blastwave when this has a Lorentz factor Γ_2, so that: $\Gamma_1/75 < \Gamma_2 < \Gamma_1$. In this context, the time offset of 19.0 ± 2.4 s before the GRB would correspond to the explosion time in the detector rest frame, while the GRB onset would mark the beginning of the γ-ray emission due to the deceleration of the fireball. From the explosion, onset and peak times we infer consistent estimates of the deceleration radius, a few $\times 10^{16}\,(\Gamma_0/100)^2\,(1 + z)^{-1}$ cm.

The interpretation of the late rebrightening as the result of a density bump in the surrounding medium would explain naturally both the prompt and the late hump with a single shell. However, the possible presence of the cooling break close to the X-ray band around the peak time, combined with the remarkable flux enhancement observed, $\Delta F/F \approx 10$, makes this scenario less appealing. The occurrence of the early NIR/optical flares at 80 and 140 s after the peak of the γ-ray emission is consistent with both scenarios: either due to density enhancements of the matter encountered by the blastwave or explained by further shells catching up with it. Finally, we note that the early (late) NIR/optical pulses do not peak contemporaneously with the corresponding γ-ray (X-ray) pulses, but are delayed by a factor of ~3 (~2) in time. A clear interpretation of this effect is lacking.

References

Akerlof, C., Balsano, R., Barthelmy, S., et al. 1999, Nature, 398, 400
Arabadjis, J. S., & Bregman, J. N. 1999, ApJ, 510, 806
Barthelmy, S. D., Chincarini, G., Burrows, D. N., et al. 2005, Nature, 438, 994
Baumgartner, W. H., & Mushotzky, R. F. 2006, ApJ, 639, 929
Bloom, J. S. 2007, GCN Circ., 6191
Burrows, D. N., Romano, P., Falcone, A., et al. 2005, Science, 309, 1833
Campana, S., Tagliaferri, G., Lazzati, D., et al. 2006, A&A, 454, 113
Cardelli, J. A., Clayton, G. C., & Mathis, J. S. 1989, ApJ, 345, 245
Cash, W. 1979, ApJ, 228, 939
Cenko, S. B., Kasliwal, M., Harrison, F. A., et al. 2006, ApJ, 652, 490
Cenko, S. B. 2007, GCN Circ., 6196
Chincarini, G., Moretti, A., Romano, P., et al. 2007, ApJ, in press [arXiv:astro-ph/0702371]
Costa, E., Frontera, F., Heise, J., et al. 1997, Nature, 387, 783
Covino, S., Stefanon, M., Sciuto, G., et al. 2004, Proc. SPIE, 5492, 1613
Covino, S., Antonelli, L. A., Calzoletti, L., et al. 2007, GCN Circ., 6190
Cusumano, G., Mangano, V., Chincarini, G., et al. 2007, A&A, 462, 73
Dai, X., Garnavich, P., Pogge, R., et al. 2007, GCN Circ., 6219
Dermer, C. D. 2004, ApJ, 614, 284
Dermer, C. D. 2007a, ApJ, 664, 384
Dermer, C. D. 2007b, ApJ, submitted [arXiv:astro-ph/0703223]
Dermer, C. D., & Mitman, K. E. 1999, ApJ, 513, L5
Devillard, N. 2001, ASP Conf. Ser., 238, 525
Falcone, A. D., Burrows, D. N., Lazzati, D., et al. 2006, ApJ, 641, 1010
Fenimore, E. E., Madras, C. D., & Nayakshin, S. 1996, ApJ, 473, 998
Fishman, G. J., & Meegan, C. A. 1995, ARA&A, 33, 415
Fox, D. W., Yost, S. A., Kulkarni, S. R., et al. 2003, Nature, 422, 284
Fukugita, M., Shimasaku, K., & Ichikawa, T. 1995, PASP, 107, 945
Galama, T. J., Groot, P. J., van Paradijs, J., et al. 1998, ApJ, 497, L13
Garnavich, P., Dai, X., Pogge, R., et al. 2007, GCN Circ., 6245
Gehrels, N., Chincarini, G., Giommi, P., et al. 2004, ApJ, 611, 1005
Ghisellini, G., Ghirlanda, G., Nava, L., & Firmani, C. 2007, ApJ, 658, L75
Granot, J., & Kumar, P. 2006, MNRAS, 366, L13
Guidorzi, C., Romano, P., Moretti, A., & Vergani, S. D. 2007a, GCN Circ., 6192
Guidorzi, C., Romano, P., Vergani, S. D., et al. 2007b, GCN Rep., 41.1
Halpern, J. P., & Armstrong, E. 2007a, GCN Circ., 6195
Halpern, J. P., & Armstrong, E. 2007b, GCN Circ., 6199
Halpern, J. P., & Armstrong, E. 2007c, GCN Circ., 6203
Halpern, J. P., & Armstrong, E. 2007d, GCN Circ., 6208
Holland, S. T., et al. 2007, GCN Circ., 6194
Ioka, K., Kobayashi, S., & Zhang, B. 2005, ApJ, 631, 429
Ioka, K., Toma, K., Yamazaki, R., & Nakamura, T. 2006, A&A, 458, 7
Jelínek, M., & Prouza, M. 2007, GCN Circ., 6197
Kalberla, P. M. W., Burton, W. B., Hartmann, D., et al. 2005, A&A, 440, 775
Kann, D. A., Filgas, R., & Högner, C. 2007, GCN Circ., 6206
Kobayashi, S., Piran, T., & Sari, R. 1997, ApJ, 490, 92
Kumar, P., & Panaitescu, A. 2000, ApJ, 541, L51
Kumar, P., & Panaitescu, A. 2003, MNRAS, 346, 905
Landolt, A. U. 1992, AJ, 104, 340
Lazzati, D., & Perna, R. 2007, MNRAS, 375, 46
Liang, E.-W., Zhang, B. B., & Zhang, B. 2007, ApJ, submitted [arXiv:0705.1373]
Malesani, D., Covino, S., D'Avanzo, P., et al. 2007, A&A, 473, 77
Mereghetti, S., Paizis, A., Gotz, D., et al. 2007, GCN Circ., 6189
Mészáros, P. 2006, Rep. Prog. Phys., 69, 2259
Mészáros, P., Rees, M. J., & Wijers, R. A. M. J. 1998, ApJ, 499, 301
Molinari, E., Vergani, S. D., Malesani, D., et al. 2007, A&A, 469, L13
Monfardini, A., Kobayashi, S., Guidorzi, C., et al. 2006, ApJ, 648, 1125
Morrison, R., & McCammon, D. 1983, ApJ, 270, 119
Norris, J. P., Nemiroff, R. J., & Bonnell, J. T. 1996, ApJ, 459, 393
Nousek, J. A., Koveliotou, C., Grupe, D., et al. 2006, ApJ, 642, 389

O'Brien, P. T., Willingale, R., Osborne, J., et al. 2006, ApJ, 647, 1213
Panaitescu, A. 2006, MNRAS, in press [arXiv:astro-ph/0612170]
Panaitescu, A. 2007, MNRAS, in press [arXiv:astro-ph/0705.1015]
Panaitescu, A., & Kumar, P. 2007, MNRAS, 376, 1065
Pei, Y. C. 1992, ApJ, 395, 130
Piro, L., Amati, L., Antonelli, L. A., et al. 1998, A&A, 331, L41
Ramirez-Ruiz, E., & Granot, J. 2006, ApJ, submitted
    [arXiv:astro-ph/0608379]
Rees, M. J., & Mészáros, P. 1992, MNRAS, 258, 41P
Rees, M. J., & Mészáros, P. 1994, ApJ, 430, L93
Rees, M. J., & Mészáros, P. 1998, ApJ, 496, L1
Romano, P., Moretti, A., Banat, P. L., et al. 2006, A&A, 450, 59
Sari, R., & Piran, T. 1997, MNRAS, 287, 110
Sazonov, S., Molkov, S., & Sunyaev, R. 2007, Ast. Lett., in press
Schlegel, D. J., Finkbeiner, D. P., & Davis, M. 1998, ApJ, 500, 525

Shaviv, N. J., & Dar, A. 1995, MNRAS, 277, 287
Stanek, K. Z., Dai, X., Prieto, J. L., et al. 2007, ApJ, 654, L21
Tagliaferri, G., Goad, M., Chincarini, G., et al. 2005, Nature, 436, 985
Vestrand, W. T., Wren, J. A., Woźniak, P. R., et al. 2006, Nature, 442, 172
Watson, D., Reeves, J. N., Hjorth, J., et al. 2006, ApJ, 637, L69
Willingale, R., O'Brien, P. T., Osborne, J., et al. 2007, ApJ, 662, 1093
Woźniak, P. R., Vestrand, W. T., Wren, J. A., et al. 2006, ApJ, 642, L99
Wren, J., Vestrand, W. T., Woźniak, P. R., White, R., & Pergande, J. 2007, GCN
    Circ., 6198
Zerbi, F. M., Chincarini, G., Ghisellini, G., et al. 2001, Astron. Nach., 322, 275
Zhang, B. 2007, Chinese J. Astron. Astrophys., 7, 1
Zhang, B., & Mészáros, P. 2001, ApJ, 552, L35
Zhang, B., Fan, Y. Z., Dyks, J., et al. 2006, ApJ, 642, 354
Zhang, B. B., Liang, E.-W., & Zhang, B. 2007, ApJ, in press
    [arXiv:astro-ph/0612246]

Online Material

Table 1. REM *KHJz'R* and CAFOS *R* photometry of GRB 070311.

Start time (s)	End time (s)	Exposure (s)	Mag[a,b]	Instr/Filter
554	704	150	15.20 ± 0.24	REM/*K*
1281	1431	150	>15.10	REM/*K*
59	69	10	14.36 ± 0.23	REM/*H*
75	85	10	13.83 ± 0.14	REM/*H*
90	100	10	14.29 ± 0.20	REM/*H*
105	115	10	14.21 ± 0.19	REM/*H*
120	130	10	14.70 ± 0.30	REM/*H*
138	148	10	13.88 ± 0.15	REM/*H*
154	164	10	14.50 ± 0.24	REM/*H*
168	178	10	14.37 ± 0.22	REM/*H*
184	210	26	14.58 ± 0.19	REM/*H*
224	274	50	15.38 ± 0.20	REM/*H*
303	353	50	15.48 ± 0.22	REM/*H*
372	522	150	15.77 ± 0.15	REM/*H*
1099	1249	150	>16.4	REM/*H*
1826	1976	150	>16.4	REM/*H*
2536	2836	300	>17.3	REM/*H*
735	885	150	>17.10	REM/*J*
1462	1612	150	17.35 ± 0.31	REM/*J*
2188	2338	150	>17.10	REM/*J*
3198	3498	300	>17.24	REM/*J*
917	1067	150	16.1 ± 0.3	REM/*z'*
59.2	89.2	30	17.49 ± 0.22	REM/*R*
105.6	135.6	30	17.86 ± 0.21	REM/*R*
151.8	181.8	30	17.73 ± 0.19	REM/*R*
197.9	227.9	30	18.12 ± 0.27	REM/*R*
244.1	274.1	30	18.19 ± 0.35	REM/*R*
290.3	320.3	30	18.31 ± 0.35	REM/*R*
336.5	597.0	180	18.91 ± 0.24	REM/*R*
613.0	643.0	30	18.32 ± 0.34	REM/*R*
659.2	4295.6	1530	21.20 ± 0.50	REM/*R*
62 174	74 783	8400	22.57 ± 0.12	CAFOS/*R*
149 180	160 924	10 810	22.60 ± 0.08	CAFOS/*R*

[a] Values are not corrected for Galactic extinction.
[b] Errors at the 68% confidence level and upper limits (3σ) are given.